Astronomy & Astrophysics manuscript no. output
May 7, 2024

Studying geometry of the ultraluminous X-ray pulsar Swift J0243.6+6124 using X-ray and optical polarimetry

Juri Poutanen[1], Sergey S. Tsygankov[1], Victor Doroshenko[2], Sofia V. Forsblom[1], Peter Jenke[3], Philip Kaaret[6], Andrei V. Berdyugin[1], Dmitry Blinov[4,5], Vadim Kravtsov[1], Ioannis Liodakis[6], Anastasia Tzouvanou[5], Alessandro Di Marco[7], Jeremy Heyl[15], Fabio La Monaca[7,8,9], Alexander A. Mushtukov[10], George G. Pavlov[11], Alexander Salganik[12,13], Alexandra Veledina[1,16], Martin C. Weisskopf[6], Silvia Zane[14], Vladislav Loktev[1], Valery F. Suleimanov[2], Colleen Wilson-Hodge[6], Svetlana V. Berdyugina[17], Masato Kagitani[18], Vilppu Piirola[1], Takeshi Sakanoi[18], Iván Agudo[19], Lucio A. Antonelli[20,21], Matteo Bachetti[22], Luca Baldini[23,24], Wayne H. Baumgartner[6], Ronaldo Bellazzini[23], Stefano Bianchi[25], Stephen D. Bongiorno[6], Raffaella Bonino[26,27], Alessandro Brez[23], Niccolò Bucciantini[28,29,30], Fiamma Capitanio[7], Simone Castellano[23], Elisabetta Cavazzuti[31], Chien-Ting Chen[32], Stefano Ciprini[33,21], Enrico Costa[7], Alessandra De Rosa[7], Ettore Del Monte[7], Laura Di Gesu[31], Niccolò Di Lalla[34], Immacolata Donnarumma[31], Michal Dovčiak[35], Steven R. Ehlert[6], Teruaki Enoto[36], Yuri Evangelista[7], Sergio Fabiani[7], Riccardo Ferrazzoli[7], Javier A. Garcia[37], Shuichi Gunji[38], Kiyoshi Hayashida[39]⋆, Wataru Iwakiri[40], Svetlana G. Jorstad[41,12], Vladimir Karas[35], Fabian Kislat[42], Takao Kitaguchi[36], Jeffery J. Kolodziejczak[6], Henric Krawczynski[43], Luca Latronico[26], Simone Maldera[26], Alberto Manfreda[44], Frédéric Marin[45], Andrea Marinucci[31], Alan P. Marscher[41], Herman L. Marshall[46], Francesco Massaro[26,27], Giorgio Matt[25], Ikuyuki Mitsuishi[47], Tsunefumi Mizuno[48], Fabio Muleri[7], Michela Negro[49], Chi-Yung Ng[50], Stephen L. O'Dell[6], Nicola Omodei[34], Chiara Oppedisano[26], Alessandro Papitto[20], Abel L. Peirson[34], Matteo Perri[21,20], Melissa Pesce-Rollins[23], Pierre-Olivier Petrucci[51], Maura Pilia[22], Andrea Possenti[22], Simonetta Puccetti[21], Brian D. Ramsey[6], John Rankin[7], Ajay Ratheesh[7], Oliver J. Roberts[32], Roger W. Romani[34], Carmelo Sgrò[23], Patrick Slane[52], Paolo Soffitta[7], Gloria Spandre[23], Douglas A. Swartz[32], Toru Tamagawa[36], Fabrizio Tavecchio[53], Roberto Taverna[54], Yuzuru Tawara[47], Allyn F. Tennant[6], Nicholas E. Thomas[6], Francesco Tombesi[8,33,55], Alessio Trois[22], Roberto Turolla[54,14], Jacco Vink[56], Kinwah Wu[14], and Fei Xie[57,7]

(Affiliations can be found after the references)

May 7, 2024

ABSTRACT

Discovery of pulsations from a number of ultra-luminous X-ray (ULX) sources proved that accretion onto neutron stars can produce luminosities exceeding the Eddington limit by a couple of orders of magnitude. The conditions necessary to achieve such high luminosities as well as the exact geometry of the accretion flow in the neutron star vicinity are, however, a matter of debate. The pulse phase-resolved polarization measurements that became possible with the launch of the *Imaging X-ray Polarimetry Explorer* (*IXPE*) can be used to determine the pulsar geometry and its orientation relative to the orbital plane. They provide an avenue to test different theoretical models of ULX pulsars. In this paper we present the results of three *IXPE* observations of the first Galactic ULX pulsar Swift J0243.6+6124 during its 2023 outburst. We find strong variations of the polarization characteristics with the pulsar phase. The average polarization degree (PD) increases from about 5% to 15% as the flux dropped by a factor of three in the course of the outburst. The polarization angle (PA) as function of the pulsar phase shows two peaks in the first two observations, but changes to a characteristic sawtooth pattern in the remaining data set. This is not consistent with a simple rotating vector model. Assuming the existence of an additional constant polarized component, we were able to fit the three observations with a common rotating vector model and obtain constraints on the pulsar geometry. In particular, we find the pulsar angular momentum inclination with respect to the line-of-sight of $i_{\rm p}$ =15°−40°, the magnetic obliquity of $\theta_{\rm p}$ =60°−80°, and the pulsar spin position angle of $\chi_{\rm p} \approx -50°$, which significantly differs from the constant component PA of about 10°. Combining these X-ray measurements with the optical PA, we find evidence for at least a 30° misalignment between the pulsar angular momentum and the binary orbital axis.

Key words. magnetic fields – methods: observational – polarization – pulsars: individual: Swift J0243.6+6124 – stars: neutron – X-rays: binaries

1. Introduction

Ultra-luminous X-ray sources (ULXs) are non-nuclear objects found in external galaxies and exhibiting high apparent X-ray luminosities exceeding the Eddington limit for stellar-mass black holes (see, e.g., Kaaret et al. 2017; King et al. 2023, for reviews). A subset of these ULXs has been identified as X-ray pulsars, systems with highly magnetized neutron stars (NSs) undergoing accretion from a companion star (Bachetti et al. 2014; Fürst et al. 2016; Israel et al. 2017; Carpano et al. 2018; Rodríguez Castillo 2020).

The accretion flow in the vicinity of the NS surface is governed by the magnetic field which channels the accreting mat-

⋆ Deceased.

ter towards the magnetic poles. At low accretion rates, the gas decelerates at the NS surface forming hotspots that radiate in the X-ray band (Zel'dovich & Shakura 1969). At high accretion rates, the radiation-dominated shock stops the gas above the NS surface forming accretion columns (Basko & Sunyaev 1976; Lyubarskii & Syunyaev 1988; Mushtukov et al. 2015). The ULX pulsars are characterized by luminosities exceeding the Eddington limit by a factor of 10–500. It is possible to achieve such a high luminosity thanks to a reduction in the interaction cross-section between matter and radiation in a strong magnetic field (Mushtukov et al. 2015), possibly dominated by quadrupole component (Tsygankov et al. 2018; Brice et al. 2021). Alternatively, a strong beaming of radiation by disk outflows can be responsible for high apparent luminosities similarly to ULXs hosting black holes (King et al. 2001; Poutanen et al. 2007). However, the latter scenario meet obstacles in the case of strongly magnetized NSs, because the size of the magnetosphere exceeds the NS size by two orders of magnitude, reducing the strength of the outflow (Lipunov 1982; Chashkina et al. 2019). Furthermore, the observed radiation cannot be strongly beamed because of the large pulsation amplitude (Mushtukov et al. 2021; Mushtukov & Portegies Zwart 2023), implying enormous accretion rates $\gtrsim 10^{19}\,\mathrm{g\,s^{-1}}$.

Complexities in ULX pulsars studies arise from their considerable distances in external galaxies. Discovery of the first Galactic ULX pulsar Swift J0243.6+6124 (J0243 hereafter) in 2017 opened new exciting possibilities. J0243 was detected by the *Swift*/BAT (Cenko et al. 2017) and soon after pulsations at a period of 9.86 s were found with the *Swift*/XRT (Kennea et al. 2017). Kong et al. (2022) reported discovery of a cyclotron line scattering feature at the energy ≈130 keV, which implies strong surface magnetic field of $B \approx 1.5 \times 10^{13}$ G. An optical counterpart, a late Oe-type or early Be-type star, was identified as USNO-B1.0 1514+0083050 based on positional coincidence with the *Swift*/XRT source (Kennea et al. 2017; Bikmaev et al. 2017; Kouroubatzakis et al. 2017). This star appears in the Gaia Data Release 3 (DR3) catalog (id: 4656281935263644 16) at the distance determined via parallax of 5.2 kpc[1] (Bailer-Jones et al. 2021). Using this distance, the peak luminosity in the 2017 outburst was $\sim 2.5 \times 10^{39}$ erg s^{-1} (Doroshenko et al. 2018; Tsygankov et al. 2018; Wilson-Hodge et al. 2018).

Pulsar radiation was predicted to be strongly polarized (Meszaros et al. 1988). Testing this prediction became possible recently thanks to the *Imaging X-ray Polarimetry Explorer* (*IXPE*) that allows us to measure X-ray polarization in the 2–8 keV energy band. *IXPE* discovered pulse-phase dependent polarization in a number of X-ray pulsars (e.g., Doroshenko et al. 2022, 2023; Tsygankov et al. 2022, 2023; Forsblom et al. 2023; Malacaria et al. 2023; Suleimanov et al. 2023; Mushtukov et al. 2023; Heyl et al. 2024). Variations of the polarization properties with the pulsar phase allow us to constrain the pulsar geometry.

During the peak of the outburst, spectrum of J0243 was dominated by the Compton reflection component with a strong iron line associated with reflection of the primary pulsar radiation from the well formed by the inner edge of the geometrically thick super-Eddington accretion disk (Bykov et al. 2022). This interpretation was later supported by the detection of the pulsations in the iron line with the *Insight-HXMT* (Xiao et al. 2024). The reflection component is also expected to be strongly polarized (Matt 1993; Poutanen et al. 1996), providing information about the reflector geometry and observer inclination. Indeed, a strongly polarized X-ray continuum attributed to reflection was observed by *IXPE* in other types of compact X-ray sources: in two Seyfert 2 galaxies, the Circinus galaxy (Ursini et al. 2023) and NGC 1068 (Marin et al. 2024), as well as in the X-ray binary Cyg X-3 (Veledina et al. 2024). In all these cases, reflection is likely coming from a torus-like structure blocking the direct view towards the central X-ray source.

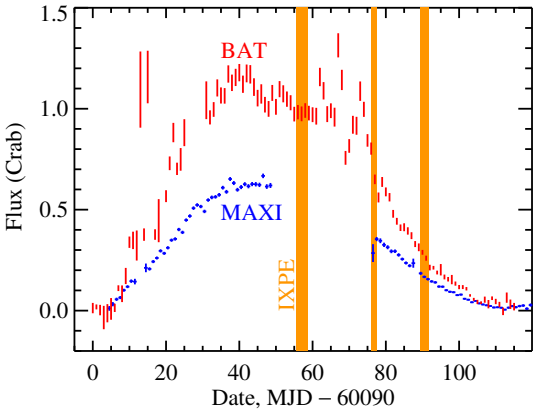

Fig. 1. Light curve of J0243 in the 2–20 and 15–50 keV energy bands obtained with the MAXI and *Swift*/BAT monitors, respectively. Vertical orange strips show the times of *IXPE* observations.

In 2023, J0243 underwent another outburst detected first with MAXI on 2023 April 8 (Setoguchi et al. 2023). A few days later, the source was localized to be J0243 with the *Swift*/XRT (Kennea et al. 2023) and subsequently 9.8 s pulsations were detected with NICER (Ng et al. 2023). The source continued to brighten, reaching peak flux in early July. The light curves of J0243 as seen by the MAXI[2] (Matsuoka et al. 2009) in the 2–20 keV energy band and *Swift*/BAT[3] (Gehrels et al. 2004) in the 15–50 keV band during the 2023 outburst are shown in Fig. 1.

In this paper we present the results of *IXPE* observations of J0243 together with accompanying optical polarimetric observations. The details of the observations and their analysis are given in Sect. 2. Constraints on the pulsar geometry are worked through in Sect. 3. We discuss the results in Sect. 4. We conclude with a summary of our findings in Sect. 5.

2. Observations and data reduction

2.1. IXPE observations

IXPE is a NASA mission in partnership with the Italian space agency (see a detailed description in Weisskopf et al. 2022), launched by a Falcon 9 rocket on 2021 December 9. There are three grazing incidence telescopes onboard the observatory. Each telescope comprises an X-ray mirror assembly and a polarization-sensitive detector unit (DU) equipped with a gas-pixel detector (GPD; Soffitta et al. 2021; Baldini et al. 2021). These instruments provide imaging polarimetry in the 2–8 keV energy band with a time resolution better than 10 μs.

IXPE observed J0243 during July 20–August 25 (ObsID 02250799), for three times on 2023 July 20–22, August 10–11, and August 23–25 with the total exposures of ≃168, 77, and 131 ks per telescope (see Fig. 1). We refer to these observations as Obs. 1, 2, and 3, respectively. The data have been processed

[1] We note that this is closer than the distance of 6.8 kpc from the Gaia DR2 catalog (Bailer-Jones et al. 2018) and used in some earlier literature.

[2] http://maxi.riken.jp/

[3] https://swift.gsfc.nasa.gov/results/transients/

Table 1. Orbital parameters of J0243 from the *Fermi*/GBM data.

Epoch of 90° mean longitude	$T_{\pi/2}$ (JED)	2458116.0970
Orbital period	$P_{\rm orb}$ (d)	27.698899
Period derivative	$\dot{P}_{\rm orb}$ (d d^{-1})	0.000000
Projected semimajor axis	$a_{\rm x} \sin i$ (lt-s)	115.531
Longitude of periastron	ω (deg)	−74.05
Eccentricity	e	0.1029

Table 2. Timing parameters used to fold *IXPE* data.

Segment	Epoch (MET)	P (s)^a	$\dot{P}$ (10^{-9} s s^{-1})^b
1	206636790.164	9.795773(3)	−1.67(3)
2	208396144.591	9.79308(1)	−1.2(1)
3	209558782.987	9.792140(5)	−2.75(6)

Notes. Folding epoch is fixed to first pulse arrival time, uncertainties are quoted at 1σ confidence level. $^{(a)}$ Pulse period. $^{(b)}$ Pulse period derivative.

with the IXPEOBSSIM package version 31.0.1 (Baldini et al. 2022) using the CalDB version 20230702:v13. Source photons were collected in a circular region with a radius $R_{\rm src} = 70''$ centered at the J0243 position. Because of the source brightness, the background was not subtracted following the recommendation by Di Marco et al. (2023). We performed the unweighted analysis (i.e. all events are taken into account independently of the quality of track reconstruction; Di Marco et al. 2022) of the *IXPE* data.

2.2. Timing

The event arrival times were corrected to the Solar system barycenter using the standard `barycorr` tool from the FTOOLS[4] package (Blackburn 1995) and accounting for the effects of binary motion using the orbital parameters from the *Fermi*/GBM[5] (see Table 1). The spin period (of $P \approx 9.79$ s) and the spin period derivative were then determined for each *IXPE* observation segment using epoch folding search, and then refined using phase-connection technique, which allows one to unambiguously define phase of each event within a given segment. The results are presented in Table 2. The gaps between individual observation segments coupled to complex evolution of intrinsic spin frequency and pulse profiles together with remaining uncertainties in orbital parameters preclude, however, direct connection of phases between the segments.

The absolute phase alignment between the segments had, therefore, be determined independently. Inspection of the pulse profile shape observed by *IXPE* (see bottom panel of Fig. 2) reveals some common features, i.e. the minimum around phase zero, several sub-peaks within the main peak, and a peak around phase 0.9 appearing late in the outburst. The observed phases of these features can thus be used to determine absolute phase offset for each segment such that all peaks/dips (determined through fitting of gaussian functions) appear at the same pulse phase. The residual scatter can then be used to assess remaining uncertainty in final phase alignment, which we estimate to be below 1%. The phase alignment can also be checked through the comparison of the observed *IXPE* pulse profiles with hard X-ray pulse profiles observed by *Fermi*/GBM.

[4] `http://heasarc.gsfc.nasa.gov/ftools`
[5] `https://gammaray.nsstc.nasa.gov/gbm/science/pulsars.html`

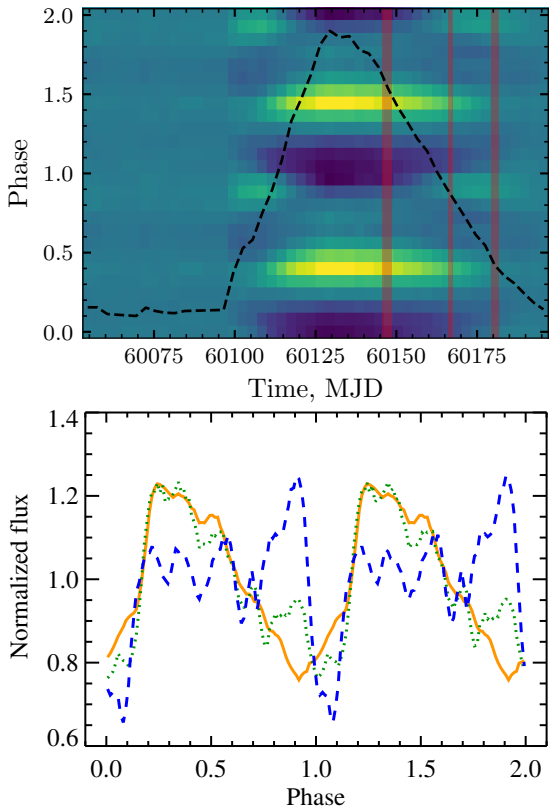

Fig. 2. Evolution of the pulse profiles during the outburst. Top: Color-coded pulse profiles as observed by *Fermi*/GBM in units of relative intensities (see Appendix A.2 in Wilson-Hodge et al. 2018) with yellow color corresponding to the maxima and dark blue to the minima of the pulse. The black dashed line shows the (pulsed) flux evolution during the outburst as seen by *Fermi*/GBM and the shaded vertical strips mark the times of *IXPE* observations. Bottom: Normalized pulse profiles in the 2–8 keV band as observed by *IXPE* in three observations and shown with the solid orange, dotted green, and dashed blue lines for Obs. 1, 2, and 3, respectively.

To do so, we used the enhanced products provided by GBM team containing Fourier coefficients of the pulse profiles for a set of time intervals with typical duration of ∼3 d. These are expected to change smoothly and since *Fermi* data contains no data gaps, the individual pulse profiles can be aligned through the cross-correlation of subsequent time intervals. The resulting pulse profile evolution is presented in the top panel of Fig. 2. We see that changes similar to those revealed by *IXPE* also occur in the GBM data, i.e. the secondary peak around phase 0.9 appears to be present only at lower luminosities and disappears at higher luminosities, i.e. our initial alignment using *IXPE* data alone proves to be robust.

2.3. Spectral analysis

For the spectral analysis, Stokes I spectra for Obs. 1, 2, and 3 were extracted using the `xpbin` tool's `PHA1` algorithm in IXPEOBBSIM, giving a set of three spectra (one for each DU) per observation. The energy spectra were binned to have at least 30 counts per energy channel. The spectra corresponding to the individual observations were fitted separately with the XSPEC package version 12.14.0 (Arnaud 1996) using χ^2 statistics. The uncertainties are given at the 68.3% confidence level. Considering the energy resolution and energy range of *IXPE*, we used a

Table 3. Spectral parameters for the best-fit model obtained with XSPEC for Obs. 1, 2, and 3.

Component	Parameter	Unit	Obs. 1	Obs. 2	Obs. 3
`tbabs`	$N_{\rm H}$	10^{22} cm^{-2}	1.60 ± 0.09	1.23 ± 0.17	0.88 ± 0.20
`bbody`	$kT_{\rm bb}$	keV	0.52 ± 0.02	0.60 ± 0.04	0.92 ± 0.03
	normalization		0.015 ± 0.001	0.008 ± 0.001	0.005 ± 0.001
`powerlaw`	Photon index		1.25 ± 0.02	0.92 ± 0.05	0.53 ± 0.12
	normalization		1.04 ± 0.04	0.37 ± 0.04	0.08 ± 0.03
`constant`	DU2		1.032 ± 0.001	1.036 ± 0.002	1.026 ± 0.002
	DU3		1.015 ± 0.001	1.018 ± 0.002	1.010 ± 0.002
	$F_{2-8\ \rm keV}{}^{a}$	10^{-9} erg cm^{-2} s^{-1}	6.7 ± 1.0	4.1 ± 0.6	1.85 ± 0.25
	$L_{2-8\ \rm keV}{}^{b}$	10^{37} erg s^{-1}	2.4	1.4	0.6
	$L_{\rm bol}{}^{c}$	10^{37} erg s^{-1}	9.1	5.3	2.3
	χ^2/d.o.f.		677.4/437	540.1/437	503.8/437

Notes. Uncertainties are given at the 68.3% (1σ) confidence level and were obtained using the `error` command in XSPEC with $\Delta\chi^2 = 1$ for one parameter of interest. [(a)] Observed flux in the 2–8 keV range. [(b)] Unabsorbed luminosity for the assumed distance of $d = 5.2$ kpc. [(c)] Total luminosity in the range 0.5–100 keV assuming bolometric correction factor of 3.8.

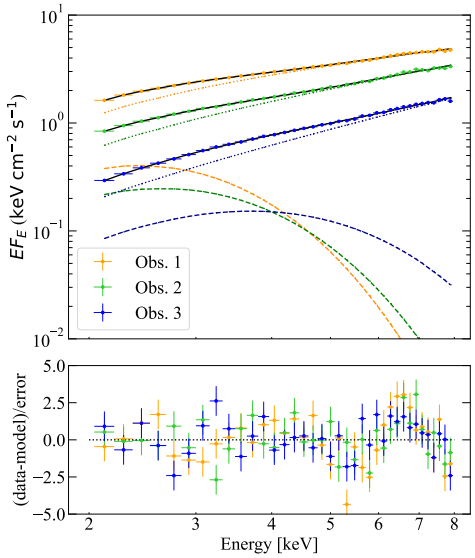

Fig. 3. *IXPE* spectra of J0243 in EF_E representation. The red, green, and blue symbols and lines correspond to Obs. 1, 2, and 3, respectively. The solid, dashed, and dotted lines show the total model spectrum, the blackbody, and the power law, respectively. The bottom panel shows the fit residuals.

simplified model consisting of of an absorbed power law plus a blackbody component to fit the J0243 spectra. To account for the interstellar absorption, a multiplicative component `tbabs` with the abundances from Wilms et al. (2000) was applied. A re-normalization constant `const` was introduced to account for possible discrepancies between effective areas of the different DUs and was fixed at unity for DU1. The full spectral model thus is

`tbabs×(bbody+powerlaw)×const`.

The results of the spectral fitting are shown in Fig. 3 and the best-fit parameters are given in Table 3. We see that the fit quality is not good, which is caused partially by systematic errors in the instrument response and partially by the presence of a weak iron line around 6.5 keV. This does not preclude us, however, from measuring the flux in the *IXPE* band. For calculations of the total luminosity we estimated the bolometric correction factor for our *IXPE* observations from the *NuSTAR* spectra at similar luminosities during the 2017 outburst (Tsygankov et al. 2018; Bykov et al. 2022). The maximum bolometric luminosity of the 2023 outburst is 10^{38} erg s^{-1}, a factor of 20 lower than the peak of the 2017 outburst (see penultimate row of Table 3).

2.4. X-ray polarimetric analysis

The polarimetric parameters of J0243 were extracted utilizing the `pcube` algorithm (`xpbin` tool) in the IXPEOBSSIM package (Baldini et al. 2022), which follows the description by Kislat et al. (2015). We derive the normalized Stokes parameters $q = Q/I$ and $u = U/I$, and subsequently the polarization degree PD= $\sqrt{q^2+u^2}$ and polarization angle PA= $\frac{1}{2}\arctan(u/q)$. The uncertainties are given at the 68.3% confidence level unless stated otherwise.

The data were divided into 24 separate pulse-phase bins. Polarization was found to be small in the 2–3 keV band. This motivated us to analyze the 3–8 keV data to reduce the noise. The evolution of the normalized Stokes parameters (q, u) is shown in Fig. 4 and their pulse-phase dependence is displayed in Fig. 5b,c. The PD (shown in Fig. 5d) grows with time, from less than 8% in Obs. 1, to ∼12% in Obs. 2 and reaches a maximum of 24% in Obs. 3. The PA (Fig. 5e) has a double peak profile in all three observations. In Obs. 1 and 2 the amplitude of variations is about 100°,[6] while in Obs. 3 the data are consistent with two full revolution by 180° during the spin period.

2.5. Optical polarization studies

IXPE observations have been accompanied by optical polarimetric observations in the *R*-band with the Robopol polarimeter located in the focal plane of the 1.3 m telescope of the Skinakas observatory (Greece). The observations were performed between 2023 July 28 and August 28 with multiple pointings. The data are presented in Table 4. We determined the intrinsic source polarization by subtracting the interstellar polarization using stars #1 and #2 (see Fig. 6), which are located ∼3′–4′ away from J0243 at a compatible distance of ∼5.7 kpc, as given by the Gaia EDR3 data (Bailer-Jones et al. 2021).

We also analyzed optical polarimetric measurements of the source during its previous outburst in 2017 obtained with DIPol-

[6] This is in strong disagreement with the recent analysis of Obs. 1 by Majumder et al. (2024), who used only 5 phase bins.

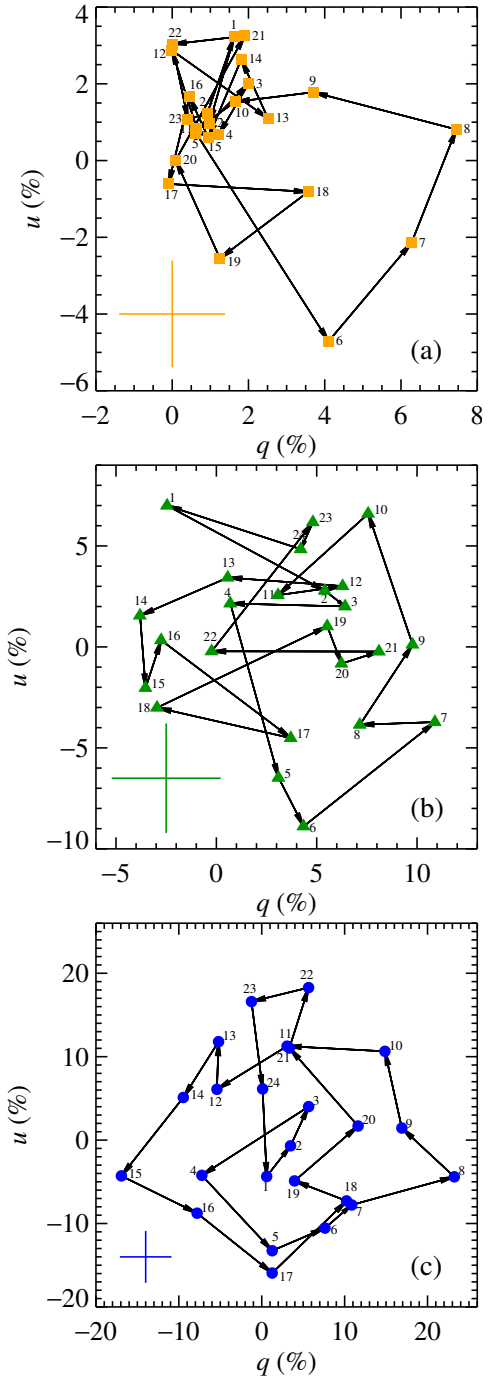

Fig. 4. Normalized Stokes parameters q and u for the phase-resolved polarimetric analysis using pcube (DUs combined), for the 3–8 keV energy band for Obs. 1 (panel a), 2 (panel b), and 3 (panel c). The typical error bar corresponding to 1σ uncertainty is shown in each panel. The phase bins are numbered. Note the different scale on separate panels.

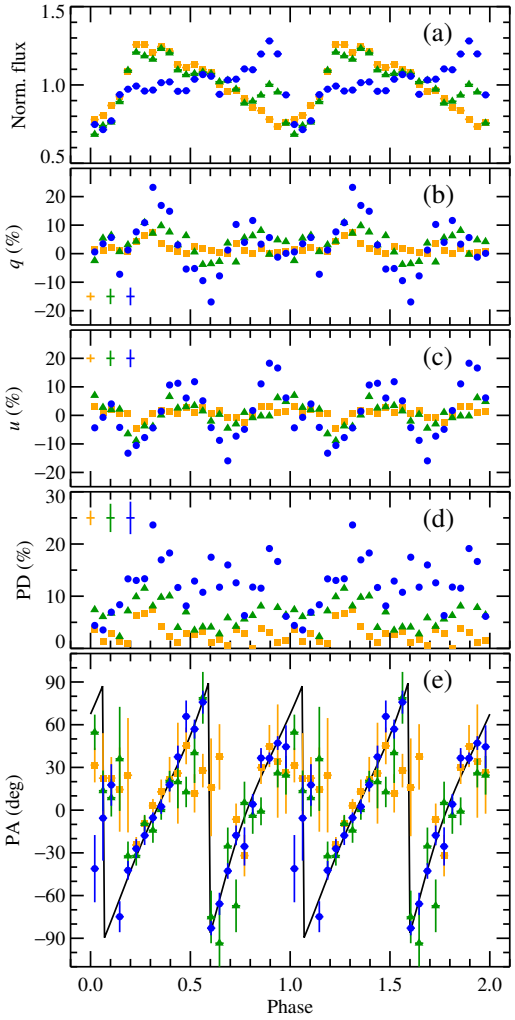

Fig. 5. Results from the pulse-phase-resolved analysis of J0243 in the 3–8 keV range, combining data from all DUs. *Panel (a)*: Pulse profile. *Panels (b)* and *(c)*: Dependence of the Stokes q and u parameters. *Panels (d)* and *(e)*: PD and PA. The data from Obs. 1, 2, and 3 are shown with the orange squares, green triangles, and blue circles, respectively. The typical error bar corresponding to 1σ uncertainty is shown in panels (b)–(d). The black solid curve is the best-fit RVM to the original PA data points (right column of Table 5).

2 (Piirola et al. 2014) at the T60 telescope at Haleakala, Hawaii (see Table A.1 in Appendix A). On average 20 measurements of polarization were taken each night. We obtained the nightly-averaged values using the 2σ-clipping method (Kosenkov et al. 2017; Kosenkov 2021). To estimate the interstellar polarization, we observed another field star #3 (see Fig. 6) which was reasonably bright and also has a parallax similar to that of the source.

The resulting normalized Stokes parameters of J0243 and the field stars are shown in Fig. 7. The intrinsic optical PD lies between ∼1% and 2.5% and the intrinsic optical PA χ_o is in the range 20°–50°, depending on the choice of the field star.

3. Pulsar geometry

3.1. RVM

Previous *IXPE* data on a number of X-ray pulsars (Doroshenko et al. 2022, 2023; Tsygankov et al. 2022, 2023; Mushtukov et al. 2023) were well described by the rotating vector model (RVM; Radhakrishnan & Cooke 1969; Meszaros et al. 1988). In this model, the evolution of the PA with pulsar phase is related to the projection of the magnetic dipole on the plane of the sky. If radiation is dominated by the ordinary-mode photons (O-mode), the PA χ is given by Eq. (30) of Poutanen (2020):

$$\tan(\chi-\chi_{\rm p}) = \frac{-\sin\theta_{\rm p}\,\sin(\phi-\phi_{\rm p})}{\sin i_{\rm p}\cos\theta_{\rm p}-\cos i_{\rm p}\sin\theta_{\rm p}\cos(\phi-\phi_{\rm p})}, \quad (1)$$

where $\chi_{\rm p}$ is the position angle (measured from north to east) of the pulsar angular momentum, $i_{\rm p}$ is the inclination of the pulsar

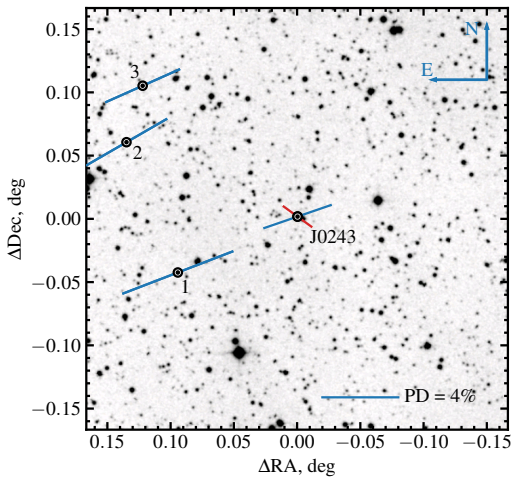

Fig. 6. Finding chart and the *R*-band polarization of J0243 (in the center) and three nearby field stars, which are situated at a similar distance according to Gaia parallaxes. The blue bars show the observed polarization of the source and field stars, while the red bar corresponds to the intrinsic polarization of the source from the Robopol observations, taking star #2 as an estimate of the interstellar contribution (see Table 4).

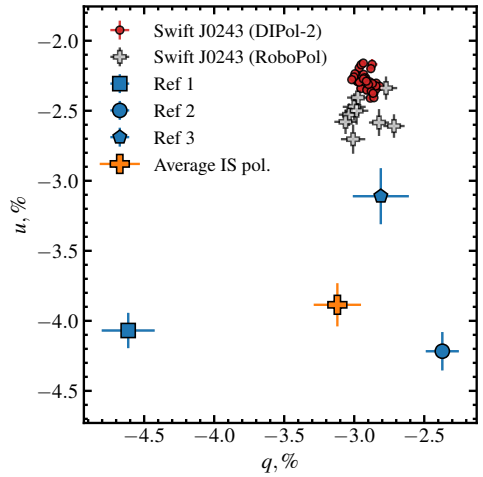

Fig. 7. Observed normalized Stokes parameters of the *R*-band optical polarization of J0243 and three nearby field stars shown in Fig. 6.

spin with respect to the line of sight, θ_p is the magnetic obliquity, i.e. the angle between the magnetic dipole and the spin axis, and ϕ_p is the phase at which the northern magnetic pole passes in front of the observer (see Fig. 8 for geometry).

If radiation is dominated by the extraordinary mode (X-mode), the PA is rotated by 90°. The general relativistic effects are significant only if the NS rotates at millisecond periods (see Poutanen 2020; Loktev et al. 2020). The RVM is also theoretically justified, because the polarization vector of the radiation produced at the magnetic poles rotates adjusting to the magnetic field geometry until the photons reach adiabatic radius at a few tens of stellar radii due to the vacuum birefringence (Heyl et al. 2003), where the magnetic field is predominantly dipole (see Sect. 4.2).

We fit the RVM to a given set of Stokes parameters (q, u) as a function of pulsar phase. The PA distribution does not conform

Table 4. Optical polarization of J0243 as observed with Robopol in 2023 in *R*-band.

Observed polarization of J0243		
HJD	q (%)	u (%)
2460153.5530	−2.97 ± 0.08	−2.41 ± 0.08
2460154.5744	−3.00 ± 0.08	−2.47 ± 0.10
2460155.5594	−2.77 ± 0.08	−2.34 ± 0.08
2460156.5468	−3.04 ± 0.07	−2.53 ± 0.08
2460157.5855	−3.06 ± 0.08	−2.58 ± 0.09
2460162.5357	−3.00 ± 0.08	−2.70 ± 0.10
2460181.5359	−2.98 ± 0.08	−2.50 ± 0.10
2460182.6066	−2.72 ± 0.08	−2.61 ± 0.08
2460184.5981	−2.82 ± 0.07	−2.58 ± 0.10
Average observed	−2.93 ± 0.03	−2.52 ± 0.03
Interstellar polarization		
Star #1	−4.61 ± 0.19	−4.07 ± 0.13
Star #2	−2.37 ± 0.12	−4.22 ± 0.14
Intrinsic polarization		
IS=star #1	1.68 ± 0.19	1.55 ± 0.13
IS=star #2	−0.56 ± 0.12	1.70 ± 0.14
	PD (%)	PA (deg)
IS=star #1	2.29 ± 0.16	21 ± 2
IS=star #2	1.79 ± 0.13	54 ± 2

Notes. Normalized Stokes parameters q and u are presented for the observed optical polarization of the source, the interstellar (IS) polarization, and the intrinsic polarization obtained by subtracting the IS polarization from the observed values. The PD and PA χ_o of the intrinsic optical polarization are computed from the intrinsic q and u. Uncertainties are 1σ.

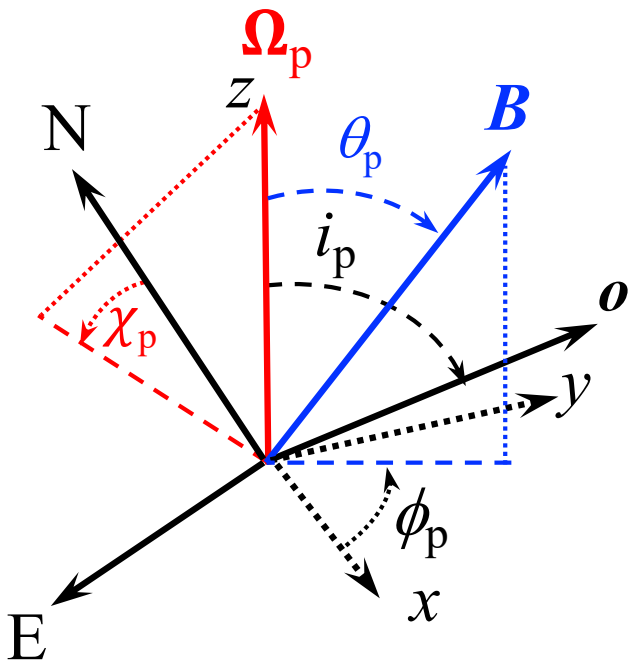

Fig. 8. Geometry of the pulsar and main parameters of the RVM. The pulsar angular momentum, $\mathbf{\Omega}_p$, makes an angle i_p with respect to the observer direction $\boldsymbol{o}$. The angle θ_p is the magnetic obliquity, i.e. the angle between magnetic dipole and the rotation axis. Pulsar phase ϕ is the azimuthal angle of vector $\boldsymbol{B}$ in the plane (x, y) perpendicular to $\mathbf{\Omega}_p$ and $\phi = \phi_p$ when $\boldsymbol{B}$, $\mathbf{\Omega}_p$, and $\boldsymbol{o}$ are coplanar. The pulsar position angle χ_p is the angle measured counterclockwise between direction to the north (N) and the projection of $\mathbf{\Omega}_p$ on the plane of the sky (N-E).

to a normal distribution, hence we use the probability density function from Naghizadeh-Khouei & Clarke (1993):

$$G(\chi) = \frac{1}{\sqrt{\pi}} \left\{ \frac{1}{\sqrt{\pi}} + \eta e^{\eta^2} \left[1 + \mathrm{erf}(\eta)\right] \right\} e^{-p_0^2/2}, \quad (2)$$

where $p_0 = \sqrt{q^2+u^2}/\sigma_\mathrm{p}$ is the 'measured' PD in units of the error, $\eta = p_0 \cos[2(\chi - \mathrm{PA})]/\sqrt{2}$, and erf is the error function. Here χ is the prediction of the RVM given by Eq. (1) for a given set of parameters and $\mathrm{PA} = \frac{1}{2}\arctan(u/q)$. The best-fit with the RVM to the pulse-phase dependent (q, u) is obtained by minimizing the log-likelihood function $\log L = -2\sum_{i,k} \ln G(\chi_{i,k})$ with the sum taken over all phase bins k for a given observation $i = 1, 2, 3$ or summing over all of them. The error on a parameter can be obtained by varying that parameter and fitting all other parameters until $\Delta \log L = 1$ is reached. We can also use a χ^2 statistics to evaluate the quality of the fit. This is possible because for highly significant detection of polarization, the PA is distributed almost normally, while the low-significance data points (when the PA distribution is far from normal) contribute very little to the χ^2.

First, we fit the RVM to individual observations. The results are given in Table 5. We find that the best-fit parameters are vastly different, e.g., the pulsar inclination for the three observations is $i_\mathrm{p} = 80°$, 60°, and 33°. We note that the corresponding χ^2 values for the best-fits are 25.1, 83.3, and 65.7 for 20 d.o.f. for Obs. 1–3, respectively. Thus, only the fit to Obs. 1 is reasonably good. If, on the other hand, we force the RVM parameters to be the same, we get the best-fit parameters of $i_\mathrm{p} = 47°$, $\theta_\mathrm{p} = 83°$, $\chi_\mathrm{p} = -67°$, and $\phi_\mathrm{p} = 0.64$ (this RVM is shown in Fig. 5e), but an unacceptable fit with $\chi^2/\mathrm{d.o.f.} = 276/68$. Thus, we find that the RVM does not provide good description of the data.

A similar situation occurred with the brightest transient pulsar observed by *IXPE*, LS V +44 17/RX J0440.9+4431, which showed the peak luminosity of 4×10^{37} erg s^{-1} (Salganik et al. 2023). In this object, significant changes in the RVM parameters were detected (Doroshenko et al. 2023). There the pulse-phase resolved Stokes q and u parameters for two epochs of observations traced similar pattern on the (q, u) plane, but the figures were shifted relative to each other. An additional, phase-independent polarized component was introduced to align the results with the RVM predictions. We now apply the same idea to the J0243 data.

3.2. Two-component polarization model

Similarly to Doroshenko et al. (2023), we assume that there are two polarized components in the J0243 data. The first one is associated with the pulsar and is described by the RVM. The second one is independent of the pulsar phase. We express the absolute Stokes parameters for each observation as a sum of the variable and constant components:

$$\begin{aligned} I(\phi) &= I_\mathrm{c} + I_\mathrm{p}(\phi), \\ Q(\phi) &= Q_\mathrm{c} + P_\mathrm{p}(\phi) I_\mathrm{p}(\phi) \cos[2\chi(\phi)], \\ U(\phi) &= U_\mathrm{c} + P_\mathrm{p}(\phi) I_\mathrm{p}(\phi) \sin[2\chi(\phi)]. \end{aligned} \quad (3)$$

Here we consider the observed Stokes parameters I, Q, and U to be scaled to the average flux value with indices denoting the constant (c) and pulsed (p) components. The PD of the variable component is P_p and its PA χ is given by Eq. (1). The scaled Stokes parameters of the constant component $(Q_\mathrm{c}, U_\mathrm{c})$ are related to the PD, P_c, and the flux, I_c, as

$$Q_\mathrm{c} = P_\mathrm{c} I_\mathrm{c} \cos(2\chi_\mathrm{c}), \quad U_\mathrm{c} = P_\mathrm{c} I_\mathrm{c} \sin(2\chi_\mathrm{c}), \quad (4)$$

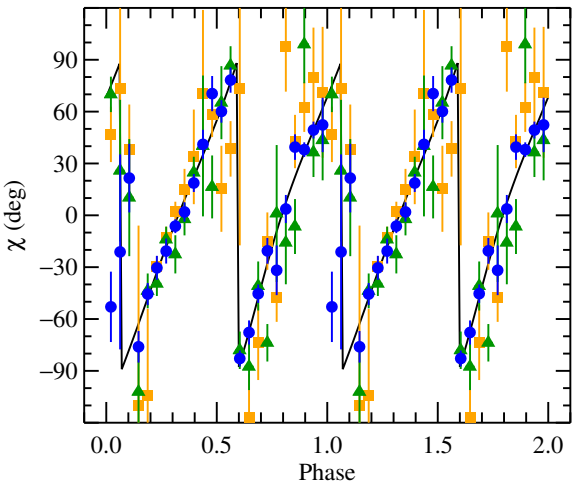

Fig. 9. Pulse-phase variations of the PA of the variable (pulsar) components after subtracting the best-fit constant polarized component from the observed Stokes parameters. The orange squares, green triangles, and blue circles with error bars correspond to Obs. 1, 2, and 3, respectively. The black line is the best-fit RVM from the two-component model (see lower part of Table 6) to all three data sets.

with its PA being $\chi_\mathrm{c} = \frac{1}{2}\arctan(U_\mathrm{c}/Q_\mathrm{c})$.

We assume that the pulsar geometry (i.e. RVM parameters) does not change between the observations and the observed changes in the polarization properties are related to the presence of an additional unpulsed polarized component. In order to describe the data from all three observations, in addition to the four RVM parameters, we introduce 6 additional free parameters $Q_{\mathrm{c},i}$ and $U_{\mathrm{c},i}$, $i = 1, 2, 3$, which describe properties of this constant component. For a given set of $Q_{\mathrm{c},i}$ and $U_{\mathrm{c},i}$, we can construct the differences $Q_\mathrm{p} = Q(\phi) - Q_\mathrm{c}$, $U_\mathrm{p} = U(\phi) - U_\mathrm{c}$, which are fit by the RVM using maximum likelihood function with the probabilities given by Eq. (2). The best-fit RVM parameters as well as the Stokes parameters of the constant component are given in the top part of Table 6. The quality of the fit is much better than with the RVM model alone, but the reduced χ^2 still exceeds 2.

The obtained Stokes parameters of the constant component correspond to the polarized fluxes (in units of the average flux) of $P_{\mathrm{c},i} I_{\mathrm{c},i} = \sqrt{Q_{\mathrm{c},i}^2 + U_{\mathrm{c},i}^2}$ in the range ~1%–4%. Once the best-fit parameters of the constant component are determined, we can obtain the value of the PA for the variable component using Eqs. (3):

$$\chi(\phi) = \frac{1}{2} \arctan\left[\frac{U(\phi) - U_\mathrm{c}}{Q(\phi) - Q_\mathrm{c}}\right]. \quad (5)$$

We find that the PA values of the constant component $\chi_{\mathrm{c},i}$ for the three observations are the same within the errors. This motivates us to perform another fit with the fixed χ_c for all three observations (this reduces the number of free parameters by 2). We refitted the data by varying, in addition to the four RVM parameters, three polarized fluxes $P_{\mathrm{c},i} I_{\mathrm{c},i}$ and the PA χ_c. The best-fit parameters are presented in the bottom part of Table 6. We see that the quality of the fit is not getting much worse in terms of the χ^2 values. The PA of the varying component associated with the pulsar as obtained using Eq. (5) are plotted in Fig. 9 together with the best-fit RVM. In order to obtain the covariance plot for these model parameters we used the affine invariant Markov chain Monte Carlo ensemble sampler EMCEE package of PYTHON (Foreman-Mackey et al. 2013). The resulting distributions are shown in Fig. 10.

Table 5. Best-fit RVM parameters for the three *IXPE* observations.

Parameter	Obs. 1	Obs. 2	Obs. 3	Obs. 1–3
i_p (deg)	80 ± 3	60 ± 5	33^{+6}_{-8}	47^{+3}_{-4}
θ_p (deg)	87 ± 2	88 ± 3	75^{+4}_{-6}	83 ± 2
χ_p (deg)	-70 ± 4	-87 ± 7	-66 ± 7	-67 ± 4
$\phi_p/(2\pi)$	0.70 ± 0.01	0.60 ± 0.03	0.65 ± 0.02	0.64 ± 0.01
χ^2/dof	25.1/20	83.3/20	65.7/20	276/68

Notes. Uncertainties on parameters correspond to $\Delta \log L = 1$ and are equivalent to 1σ.

Table 6. Best-fit parameters of the two-component model.

Parameter	Obs. 1	Obs. 2	Obs. 3
i_p (deg)		40^{+9}_{-11}	
θ_p (deg)		80^{+4}_{-5}	
χ_p (deg)		-45^{+16}_{-10}	
$\phi_p/(2\pi)$		$0.70^{+0.05}_{-0.03}$	
Q_c (%)	1.3 ± 0.4	$3.4^{+1.0}_{-0.8}$	$1.9^{+2.3}_{-1.3}$
U_c (%)	0.7 ± 0.4	-0.6 ± 0.9	-1.6 ± 1.7
χ_c (deg)	14 ± 8	-5 ± 8	-20 ± 21
$P_c I_c$ (%)	1.4 ± 0.4	3.4 ± 0.9	2.5 ± 1.8
χ^2/dof		150/62	
Same PA for constant component			
i_p (deg)		29^{+9}_{-15}	
θ_p (deg)		76^{+5}_{-15}	
χ_p (deg)		-49^{+12}_{-11}	
$\phi_p/(2\pi)$		0.68 ± 0.03	
χ_c (deg)		8 ± 7	
$P_c I_c$ (%)	1.5 ± 0.4	3.1 ± 0.7	1.5 ± 1.0
χ^2/dof		156/64	

Notes. Uncertainties on parameters correspond to $\Delta \log L = 1$ and are equivalent to 1σ.

4. Discussion

4.1. System geometry and origin of constant polarized component

Our fits demonstrated that polarization cannot be described with a simple RVM. The main reason is that while the PA makes two full turns (by 180°) during one pulsar period during Obs. 3, it shows a double sine wave during Obs. 1 and 2. Such a behavior contradicts the RVM. Furthermore, the quality of the fit is rather bad and the best-fit pulsar geometrical parameters vary strongly between observations (see Table 5).

Following Doroshenko et al. (2023), we assumed that in addition to the direct pulsar radiation described by the RVM, there a pulse-phase-independent polarized component. The data are much better described by this two-component model with a constant set of RVM parameters. The PA of the constant component was consistent to be the same (between −20° and 14°) within the errors in the three observations. Fixing this PA at the same value gave the best-fit value of $\chi_c = 8° \pm 7°$. We found that the polarized flux (in units of the average flux) of the constant component $P_c I_c$ is between 1.5% and 3%. Because the contribution of this component to the total flux is unknown, the value of P_c is not well determined. The lower limit on P_c comes from the fact that the flux of the constant component cannot exceed the flux minimum of around 60% of the average flux (see Fig. 1). This results in $P_c \gtrsim 3.5$–5% depending on the observation, with the value growing inversely proportional to I_c. A lower limit on I_c comes from the condition $P_c < 100\%$, which translates to $I_c \gtrsim 1.5$–3%. If we assume more realistically that $P_c \lesssim 30\%$ (see below), then $I_c \gtrsim 5$–10%.

The constant component can be associated with scattering in equatorial accretion disk wind (Doroshenko et al. 2023). If the wind half-opening angle is 30°, it occupies half of the sky as seen from the central source. Thus for the Thomson optical depth through the wind of 0.2, 10% of pulsar radiation is scattered by the wind. The PD of the scattered component depends on the disk inclination as $\approx \sin^2 i_d/(3 - \cos^2 i_d)$ (Sunyaev & Titarchuk 1985; Nitindala et al. in prep.). For $i_d > 60°$, the PD is close to 30% and the polarized flux in that case has to be around 3% of the average flux consistent with the data. At lower i_d, a larger contribution of this component to the average flux is required.

The PA of the constant X-ray component is ∼10° (or −170°). If its polarization is produced in the accretion disk wind, it is natural to assume that the PA is related to the position angle of the accretion disk axis. On the other hand, polarization in the optical band is likely produced by scattering of the Be-star radiation off the decretion disk (which occupies a much larger solid angle than the accretion disk around a NS) and therefore provides orientation of that disk. Because of the uncertainty in the value of the IS polarization, the intrinsic optical PA χ_o is in the range between 20° and 50° (see Tables 4 and A.1). The lowest value of χ_o (corresponding to the closest star #1 as a proxy for IS polarization) is within 2σ from χ_c, while the highest PA is clearly inconsistent with that. Thus, there is an indication that the accretion and decretion disks are somewhat misaligned.

From the two-component model fit, we constrained the pulsar inclination at $i_p \approx 15°-40°$ and the magnetic obliquity to $\theta_p \approx 60°-80°$. The pulsar rotation axis' position angle is $\chi_p \approx -50° \pm 10°$, which is clearly inconsistent with the PA of the constant component χ_c. If pulsar radiation escapes in the X-mode, then $\chi_p \approx 40°$ (or −140°), which is still far from χ_c. Under an assumption that χ_c gives the orientation of the accretion disk (and the binary orbit), the difference $|\chi_p - \chi_c|$ is related to the misalignment angle between the pulsar spin axis and the orbital axis, which is then about 30°–50°.

We note that evidence for a misalignment was found also in other pulsars. For example, in LS V +44 17 (Doroshenko et al. 2023), we found $\chi_o \approx \chi_c \sim 60°-70°$ and both were inconsistent with $\chi_p \approx -10°$ implying a misalignment of ∼75° if the pulsar emits predominantly in the O-mode or at least 15° (for emission in the X-mode). In Her X-1 (Doroshenko et al. 2022; Heyl et al. 2024), the misalignment is at least 25°, but can be ∼65° or even higher.

Finally, we note that the quality of the fit with the two-component model is still not statistically acceptable, likely indicating that the actual physical situation is even more complex. The polarization properties of the additional component may

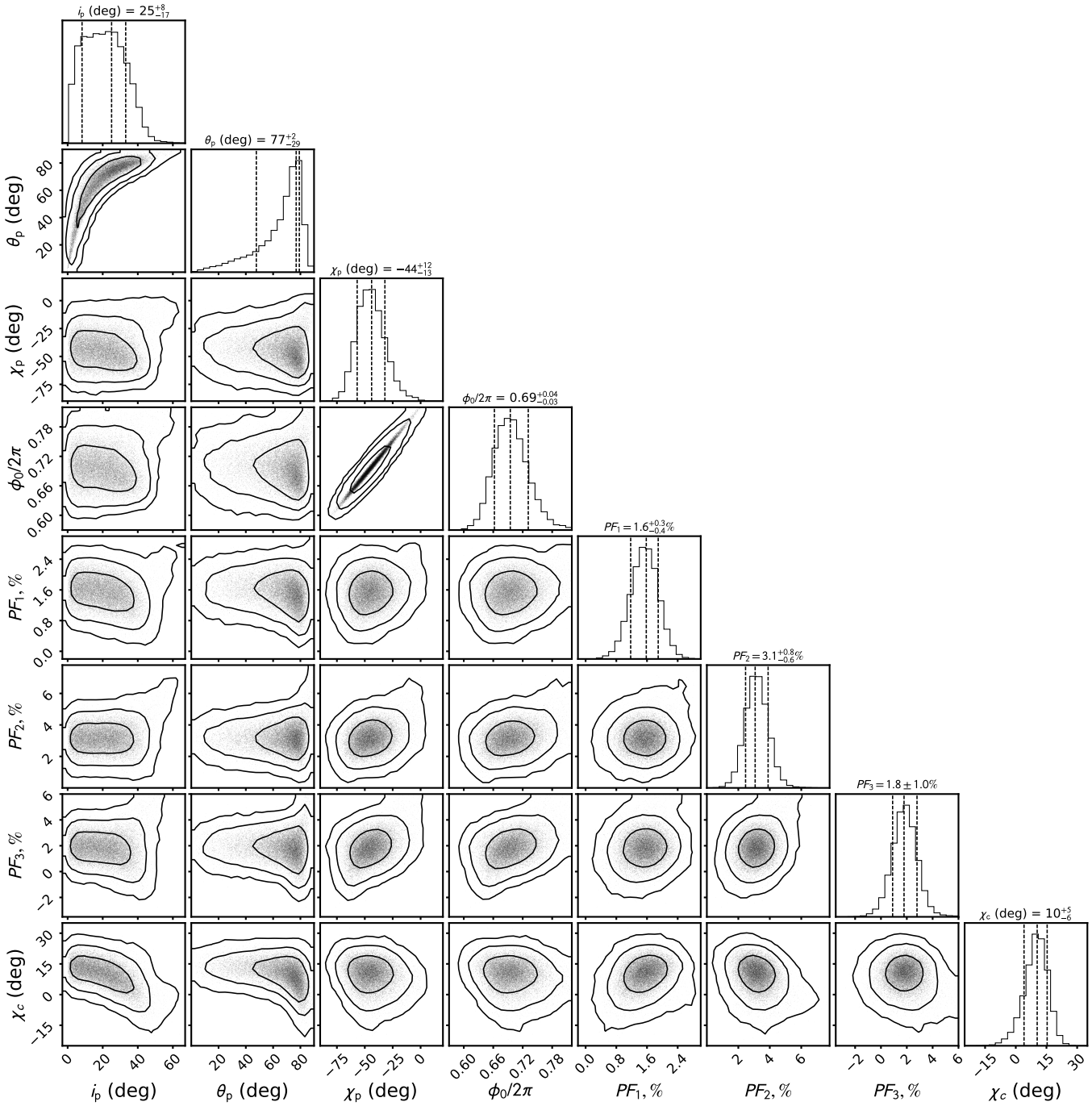

Fig. 10. Corner plot of the posterior distribution for parameters of the RVM plus a constant model with one free PA given by Eqs. (3) fitted directly to the (q, u) values using likelihood function (2). Here PF_i, i = 1, 2, and 3 is the polarized flux $P_c I_c$ of the constant component (measured in units of the average flux) during Obs. 1, 2, and 3, respectively, and χ_c is its polarization angle. The two-dimensional contours correspond to 68.3%, 95.45% and 99.73% confidence levels. The histograms show the normalized one-dimensional distributions for a given parameter derived from the posterior samples.

vary with the pulsar phase somehow, but not with the amplitude comparable to that of the pulsar itself. For example, scattering in the wind can be phase-dependent because of the azimuthal asymmetry of the pulsar radiation.

4.2. Polarization – flux anti-correlation

Our fits demonstrate that most of the polarized flux is produced by the pulsating component. Furthermore, the observed polarization has a clear trend of increasing PD with decreasing flux. What would be the most probable reason for such a behavior?

At low luminosities when most of the radiation is produced in two small hotspots at the NS surface close to the magnetic poles, the PD is determined by the structure of the atmosphere and the energy dissipation profile (Doroshenko et al. 2022). The PD is conserved when photons propagate through the magnetosphere and the polarization vector adjusts to the orientation of the magnetic field until the adiabatic radius is reached (e.g., Heyl & Shaviv 2002; Taverna et al. 2015). The adiabatic radius as a

function of photon energy E is (Heyl & Caiazzo 2018)

$$R_{\rm ad}(E) \sim 3.5\times10^7 \left(\frac{E}{1\,{\rm keV}}\right)^{1/5} \left(B_{13}R_6^3\right)^{2/5}\ {\rm cm}, \quad (6)$$

where B_{13} is the surface magnetic field strength in units of 10^{13} G and R_6 is the NS radius in units of 10^6 cm. For the surface magnetic field of $B_{13} \approx 1$ (Kong et al. 2022) and $R_6 \approx 1.2$ (e.g., Nättilä et al. 2017; Miller et al. 2020; Annala et al. 2022), it exceeds the NS radius for photons in the IXPE range by more than an order of magnitude. At this distance, the magnetic field is mostly dipole resulting in the PA that follows the RVM, as indeed observed in a number of X-ray pulsars (Doroshenko et al. 2022; Malacaria et al. 2023; Tsygankov et al. 2023; Suleimanov et al. 2023; Mushtukov et al. 2023; Heyl et al. 2024).

At a luminosity close to 10^{38} erg s^{-1}, a number of additional effects come into play. Firstly, the emission region is not point-like anymore, but radiation is produced in an accretion column, which stands above the NS surface. Locally, the polarization direction correlates with the magnetic field direction. However, the PD of the whole column radiation can be smaller that the local values, because of the different energy dissipation profile, varying depth of the vacuum resonance, and resulting mode conversions (Lai & Ho 2003; Doroshenko et al. 2022; Lai 2023). Secondly, a substantial part of the column radiation illuminates the NS surface and is reflected from that (Lyubarskii & Syunyaev 1988; Poutanen et al. 2013). Because of varying magnetic field directions across the NS surface and different relative contributions of the O- and X-modes in the reflected radiation, the total PD is reduced.

And finally, the accretion flow is expected to be optically thick (Mushtukov et al. 2017, 2019) within the NS magnetospheric radius

$$R_{\rm m} \simeq 3.4\times10^8\,\Lambda\,B_{13}^{4/7}\dot{M}_{18}^{-2/7}m^{-1/7}R_6^{12/7} \approx 2.2\times10^8\,{\rm cm}, \quad (7)$$

where Λ is coefficient typically taken to be ~ 0.5 for the case of disk accretion (Chashkina et al. 2019), $\dot{M}_{18}$ is the mass accretion rate in units of 10^{18} g s^{-1}, and $m \approx 1.5$ is the mass of a NS in solar masses. Under this condition, a substantial fraction of X-ray photons emitted close the NS surface is reprocessed by the optically think envelope created around the NS magnetospheric cavities. Because the size of the magnetosphere exceeds the adiabatic radius, the final polarization of X-ray photons is defined by scattering off the envelope. The PD and PA will depend more on the scattering geometry rather than on the projection of the NS magnetic dipole on the sky. Integrating the Stokes parameters over the envelope, significantly reduces the total PD. Thus in this model, the observed anticorrelation of the PD and flux is a result of variable optical thickness of the envelope: the larger the mass accretion rate and the flux, the larger the optical thickness of envelope and, thus, the larger the fraction of photons experiencing reprocessing by the envelope outside the NS adiabatic radius that reduces the PD.

5. Summary

Swift J0243.6+6124 was observed by *IXPE* in July–August of 2023 three times during its outburst. The main results of our study of its polarimetric properties can be summarized as follows:

1. Using updated pulsar ephemeris from *Fermi*/GBM we were able to phase connect the pulse arrival times for the whole duration of the outburst.
2. The phase-resolved polarimetric analysis revealed a significant detection of X-ray polarization with the PD reaching ∼6%, 10%, and 20% during the three observations separated by a month when the flux dropped by a factor of three.
3. We showed that evolution of the PA with pulsar phase in Obs. 1 and 2 having double sine-wave structure is inconsistent with the RVM. This brought us to the conclusion that the likely reason for this discrepancy is the presence of the phase-independent polarized component produced, for example, by scattering in the accretion disk wind as was proposed for another bright X-ray pulsar LS V +44 17 (Doroshenko et al. 2023).
4. Assuming the same RVM parameters for the three observations, we fitted the data with the two-component model and obtained the PA of the constant component $\chi_{\rm c}$ between $-20°$ and $15°$. Assuming that the PA for all observations is the same, we get $\chi_{\rm c} = 8° \pm 7°$. Also assuming that the constant component contributes 10% of the average flux, we get the PD of that component varies between 15% and 30%. We estimated the inclination of the NS rotation axis to the line of sight of $i_{\rm p} = 15°-40°$, the magnetic obliquity of $\theta_{\rm p} = 60°-80°$, and the pulsar position angle of $\chi_{\rm p} \approx -50°$.
5. Using optical polarimetric observations of the source and nearby field stars, we determined the intrinsic PA $\chi_{\rm o}$ to lie between $20°$ and $50°$, depending on the choice of a field star to estimate the contribution of the interstellar component. The lowest value of $\chi_{\rm o}$ is consistent with $\chi_{\rm c}$ within 2σ, while the higher PA are clearly inconsistent with that. Associating optical polarization with scattering in the decretion disk, the data indicate a possible misalignment between accretion and decretion disks axes.
6. A deviation of $\chi_{\rm c}$ from the pulsar position angle $\chi_{\rm p}$ implies a $\gtrsim 30°$ misalignment between pulsar rotation axis and the orbital (accretion disk) axis.

Acknowledgements. The Imaging X-ray Polarimetry Explorer (IXPE) is a joint US and Italian mission. The US contribution is supported by the National Aeronautics and Space Administration (NASA) and led and managed by its Marshall Space Flight Center (MSFC), with industry partner Ball Aerospace (contract NNM15AA18C). The Italian contribution is supported by the Italian Space Agency (Agenzia Spaziale Italiana, ASI) through contract ASI-OHBI-2022-13-I.0, agreements ASI-INAF-2022-19-HH.0 and ASI-INFN-2017.13-H0, and its Space Science Data Center (SSDC) with agreements ASI-INAF-2022-14-HH.0 and ASI-INFN 2021-43-HH.0, and by the Istituto Nazionale di Astrofisica (INAF) and the Istituto Nazionale di Fisica Nucleare (INFN) in Italy. This research used data products provided by the IXPE Team (MSFC, SSDC, INAF, and INFN) and distributed with additional software tools by the High-Energy Astrophysics Science Archive Research Center (HEASARC), at NASA Goddard Space Flight Center (GSFC). This research has been supported by the Academy of Finland grants 333112, 349144 and 355672 (JP, SST, AV), the German Academic Exchange Service (DAAD) travel grant 57525212 (VD, VFS), UKRI Stephen Hawking fellowship (AAM), Natural Sciences and Engineering Research Council of Canada (JH), and Deutsche Forschungsgemeinschaft (DFG) grant WE 1312/59-1 (VFS). I.L. was supported by the NASA Postdoctoral Program at the Marshall Space Flight Center, administered by Oak Ridge Associated Universities under contract with NASA. Nordita is supported in part by NordForsk.

References

Annala, E., Gorda, T., Katerini, E., et al. 2022, Physical Review X, 12, 011058
Arnaud, K. A. 1996, in ASP Conf. Ser., Vol. 101, Astronomical Data Analysis Software and Systems V, ed. G. H. Jacoby & J. Barnes (San Francisco: Astron. Soc. Pac.), 17
Bachetti, M., Harrison, F. A., Walton, D. J., et al. 2014, Nature, 514, 202
Bailer-Jones, C. A. L., Rybizki, J., Fouesneau, M., Demleitner, M., & Andrae, R. 2021, AJ, 161, 147
Bailer-Jones, C. A. L., Rybizki, J., Fouesneau, M., Mantelet, G., & Andrae, R. 2018, AJ, 156, 58

Baldini, L., Barbanera, M., Bellazzini, R., et al. 2021, Astroparticle Physics, 133, 102628
Baldini, L., Bucciantini, N., Lalla, N. D., et al. 2022, SoftwareX, 19, 101194
Basko, M. M., & Sunyaev, R. A. 1976, MNRAS, 175, 395
Bikmaev, I., Shimansky, V., Irtuganov, E., et al. 2017, The Astronomer's Telegram, 10968, 1
Blackburn, J. K. 1995, in ASP Conf. Ser., Vol. 77, Astronomical Data Analysis Software and Systems IV, ed. R. A. Shaw, H. E. Payne, & J. J. E. Hayes (San Francisco: Astron. Soc. Pac.), 367
Brice, N., Zane, S., Turolla, R., & Wu, K. 2021, MNRAS, 504, 701
Bykov, S. D., Gilfanov, M. R., Tsygankov, S. S., & Filippova, E. V. 2022, MNRAS, 516, 1601
Carpano, S., Haberl, F., Maitra, C., & Vasilopoulos, G. 2018, MNRAS, 476, L45
Cenko, S. B., Barthelmy, S. D., D'Avanzo, P., et al. 2017, GRB Coordinates Network, 21960, 1
Chashkina, A., Lipunova, G., Abolmasov, P., & Poutanen, J. 2019, A&A, 626, A18
Di Marco, A., Costa, E., Muleri, F., et al. 2022, AJ, 163, 170
Di Marco, A., Soffitta, P., Costa, E., et al. 2023, AJ, 165, 143
Doroshenko, V., Tsygankov, S., & Santangelo, A. 2018, A&A, 613, A19
Doroshenko, V., Poutanen, J., Tsygankov, S. S., et al. 2022, Nature Astronomy, 6, 1433
Doroshenko, V., Poutanen, J., Heyl, J., et al. 2023, A&A, 677, A57
Foreman-Mackey, D., Hogg, D. W., Lang, D., & Goodman, J. 2013, PASP, 125, 306
Forsblom, S. V., Poutanen, J., Tsygankov, S. S., et al. 2023, ApJ, 947, L20
Fürst, F., Walton, D. J., Harrison, F. A., et al. 2016, ApJ, 831, L14
Gehrels, N., Chincarini, G., Giommi, P., et al. 2004, ApJ, 611, 1005
Heyl, J., & Caiazzo, I. 2018, Galaxies, 6, 76
Heyl, J., Doroshenko, V., González-Caniulef, D., et al. 2024, Nature Astronomy, in press, arXiv:2311.03667
Heyl, J. S., & Shaviv, N. J. 2002, Phys. Rev. D, 66, 023002
Heyl, J. S., Shaviv, N. J., & Lloyd, D. 2003, MNRAS, 342, 134
Israel, G. L., Belfiore, A., Stella, L., et al. 2017, Science, 355, 817
Kaaret, P., Feng, H., & Roberts, T. P. 2017, ARA&A, 55, 303
Kennea, J. A., Bahramian, A., & Negoro, H. 2023, The Astronomer's Telegram, 15984, 1
Kennea, J. A., Lien, A. Y., Krimm, H. A., Cenko, S. B., & Siegel, M. H. 2017, The Astronomer's Telegram, 10809, 1
King, A., Lasota, J.-P., & Middleton, M. 2023, New A Rev., 96, 101672
King, A. R., Davies, M. B., Ward, M. J., Fabbiano, G., & Elvis, M. 2001, ApJ, 552, L109
Kislat, F., Clark, B., Beilicke, M., & Krawczynski, H. 2015, Astroparticle Physics, 68, 45
Kong, L.-D., Zhang, S., Zhang, S.-N., et al. 2022, ApJ, 933, L3
Kosenkov, I. A. 2021, Dipol2Red: Linear polarization data reduction pipeline for DIPol-2 and DIPol-UF polarimeters
Kosenkov, I. A., Berdyugin, A. V., Piirola, V., et al. 2017, MNRAS, 468, 4362
Kouroubatzakis, K., Reig, P., Andrews, J., & Zezas, A. 2017, The Astronomer's Telegram, 10822, 1
Lai, D. 2023, Proceedings of the National Academy of Science, 120, e2216534120
Lai, D., & Ho, W. C. G. 2003, ApJ, 588, 962
Lipunov, V. M. 1982, Soviet Ast., 26, 54
Loktev, V., Salmi, T., Nättilä, J., & Poutanen, J. 2020, A&A, 643, A84
Lyubarskii, Y. E., & Syunyaev, R. A. 1988, Soviet Astronomy Letters, 14, 390
Majumder, S., Chatterjee, R., Jayasury, K. M., Das, S., & Nandi, A. 2024, arXiv e-prints, arXiv:2402.11602
Malacaria, C., Heyl, J., Doroshenko, V., et al. 2023, A&A, 675, A29
Marin, F., Marinucci, A., Laurenti, M., et al. 2024, arXiv e-prints, arXiv:2403.02061
Matsuoka, M., Kawasaki, K., Ueno, S., et al. 2009, PASJ, 61, 999
Matt, G. 1993, MNRAS, 260, 663
Meszaros, P., Novick, R., Szentgyorgyi, A., Chanan, G. A., & Weisskopf, M. C. 1988, ApJ, 324, 1056
Miller, M. C., Chirenti, C., & Lamb, F. K. 2020, ApJ, 888, 12
Mushtukov, A. A., Ingram, A., Middleton, M., Nagirner, D. I., & van der Klis, M. 2019, MNRAS, 484, 687
Mushtukov, A. A., & Portegies Zwart, S. 2023, MNRAS, 518, 5457
Mushtukov, A. A., Portegies Zwart, S., Tsygankov, S. S., Nagirner, D. I., & Poutanen, J. 2021, MNRAS, 501, 2424
Mushtukov, A. A., Suleimanov, V. F., Tsygankov, S. S., & Ingram, A. 2017, MNRAS, 467, 1202
Mushtukov, A. A., Suleimanov, V. F., Tsygankov, S. S., & Poutanen, J. 2015, MNRAS, 447, 1847
Mushtukov, A. A., Tsygankov, S. S., Poutanen, J., et al. 2023, MNRAS, 524, 2004
Naghizadeh-Khouei, J., & Clarke, D. 1993, A&A, 274, 968
Nättilä, J., Miller, M. C., Steiner, A. W., et al. 2017, A&A, 608, A31
Ng, M., Sanna, A., Chakrabarty, D., et al. 2023, The Astronomer's Telegram, 15987, 1
Piirola, V., Berdyugin, A., & Berdyugina, S. 2014, in Proc. SPIE, Vol. 9147, Ground-based and Airborne Instrumentation for Astronomy V, 91478I
Poutanen, J. 2020, A&A, 641, A166
Poutanen, J., Lipunova, G., Fabrika, S., Butkevich, A. G., & Abolmasov, P. 2007, MNRAS, 377, 1187
Poutanen, J., Mushtukov, A. A., Suleimanov, V. F., et al. 2013, ApJ, 777, 115
Poutanen, J., Nagendra, K. N., & Svensson, R. 1996, MNRAS, 283, 892
Radhakrishnan, V., & Cooke, D. J. 1969, Astrophys. Lett., 3, 225
Rodríguez Castillo, G. A. 2020, ApJ, 895, 60
Salganik, A., Tsygankov, S. S., Doroshenko, V., et al. 2023, MNRAS, 524, 5213
Setoguchi, K., Negoro, H., Nakajima, M., et al. 2023, The Astronomer's Telegram, 15983, 1
Soffitta, P., Baldini, L., Bellazzini, R., et al. 2021, AJ, 162, 208
Suleimanov, V. F., Forsblom, S. V., Tsygankov, S. S., et al. 2023, A&A, 678, A119
Sunyaev, R. A., & Titarchuk, L. G. 1985, A&A, 143, 374
Taverna, R., Turolla, R., Gonzalez Caniulef, D., et al. 2015, MNRAS, 454, 3254
Tsygankov, S. S., Doroshenko, V., Mushtukov, A. A., Lutovinov, A. A., & Poutanen, J. 2018, MNRAS, 479, L134
Tsygankov, S. S., Doroshenko, V., Poutanen, J., et al. 2022, ApJ, 941, L14
Tsygankov, S. S., Doroshenko, V., Mushtukov, A. A., et al. 2023, A&A, A48
Ursini, F., Marinucci, A., Matt, G., et al. 2023, MNRAS, 519, 50
Veledina, A., Muleri, F., Poutanen, J., et al. 2024, Nature Astronomy, in press, arXiv:2303.01174
Weisskopf, M. C., Soffitta, P., Baldini, L., et al. 2022, JATIS, 8, 026002
Wilms, J., Allen, A., & McCray, R. 2000, ApJ, 542, 914
Wilson-Hodge, C. A., Malacaria, C., Jenke, P. A., et al. 2018, ApJ, 863, 9
Xiao, Y. X., Xu, Y. J., Ge, M. Y., et al. 2024, ApJ, 965, 18
Zel'dovich, Y. B., & Shakura, N. I. 1969, Soviet Ast., 13, 175

[1] Department of Physics and Astronomy, FI-20014 University of Turku, Finland e-mail: juri.poutanen@utu.fi
[2] Institut für Astronomie und Astrophysik, Universität Tübingen, Sand 1, D-72076 Tübingen, Germany
[3] University of Alabama in Huntsville, NSSTC, Huntsville, AL 35805, USA
[4] Institute of Astrophysics, Foundation for Research and Technology-Hellas, GR-70013 Heraklion, Greece
[5] Department of Physics, University of Crete, GR-70013, Heraklion, Greece
[6] NASA Marshall Space Flight Center, Huntsville, AL 35812, USA
[7] INAF Istituto di Astrofisica e Planetologia Spaziali, Via del Fosso del Cavaliere 100, 00133 Roma, Italy
[8] Dipartimento di Fisica, Università degli Studi di Roma "Tor Vergata", Via della Ricerca Scientifica 1, 00133 Roma, Italy
[9] Dipartimento di Fisica, Università degli Studi di Roma "La Sapienza", Piazzale Aldo Moro 5, 00185 Roma, Italy
[10] Astrophysics, Department of Physics, University of Oxford, Denys Wilkinson Building, Keble Road, Oxford OX1 3RH, UK
[11] Department of Astronomy and Astrophysics, Pennsylvania State University, University Park, PA 16801, USA
[12] Department of Astrophysics, St. Petersburg State University, Universitetsky pr. 28, Petrodvoretz, 198504 St. Petersburg, Russia
[13] Space Research Institute of the Russian Academy of Sciences, Profsoyuznaya Str. 84/32, Moscow 117997, Russia
[14] Mullard Space Science Laboratory, University College London, Holmbury St Mary, Dorking, Surrey RH5 6NT, UK
[15] University of British Columbia, Vancouver, BC V6T 1Z4, Canada
[16] Nordita, KTH Royal Institute of Technology and Stockholm University, Hannes Alfvéns väg 12, SE-10691 Stockholm, Sweden
[17] Istituto Ricerche Solari Aldo e Cele Daccò (IRSOL), Faculty of Informatics, Università della Svizzera italiana, 6605 Locarno, Switzerland
[18] Graduate School of Sciences, Tohoku University, Aoba-ku, 980-8578 Sendai, Japan
[19] Instituto de Astrofísica de Andalucía – CSIC, Glorieta de la Astronomía s/n, 18008 Granada, Spain
[20] INAF Osservatorio Astronomico di Roma, Via Frascati 33, 00040 Monte Porzio Catone (RM), Italy
[21] Space Science Data Center, Agenzia Spaziale Italiana, Via del Politecnico snc, 00133 Roma, Italy

[22] INAF Osservatorio Astronomico di Cagliari, Via della Scienza 5, 09047 Selargius (CA), Italy
[23] Istituto Nazionale di Fisica Nucleare, Sezione di Pisa, Largo B. Pontecorvo 3, 56127 Pisa, Italy
[24] Dipartimento di Fisica, Università di Pisa, Largo B. Pontecorvo 3, 56127 Pisa, Italy
[25] Dipartimento di Matematica e Fisica, Università degli Studi Roma Tre, via della Vasca Navale 84, 00146 Roma, Italy
[26] Istituto Nazionale di Fisica Nucleare, Sezione di Torino, Via Pietro Giuria 1, 10125 Torino, Italy
[27] Dipartimento di Fisica, Università degli Studi di Torino, Via Pietro Giuria 1, 10125 Torino, Italy
[28] INAF Osservatorio Astrofisico di Arcetri, Largo Enrico Fermi 5, 50125 Firenze, Italy
[29] Dipartimento di Fisica e Astronomia, Università degli Studi di Firenze, Via Sansone 1, 50019 Sesto Fiorentino (FI), Italy
[30] Istituto Nazionale di Fisica Nucleare, Sezione di Firenze, Via Sansone 1, 50019 Sesto Fiorentino (FI), Italy
[31] Agenzia Spaziale Italiana, Via del Politecnico snc, 00133 Roma, Italy
[32] Science and Technology Institute, Universities Space Research Association, Huntsville, AL 35805, USA
[33] Istituto Nazionale di Fisica Nucleare, Sezione di Roma "Tor Vergata", Via della Ricerca Scientifica 1, 00133 Roma, Italy
[34] Department of Physics and Kavli Institute for Particle Astrophysics and Cosmology, Stanford University, Stanford, California 94305, USA
[35] Astronomical Institute of the Czech Academy of Sciences, Boční II 1401/1, 14100 Praha 4, Czech Republic
[36] RIKEN Cluster for Pioneering Research, 2-1 Hirosawa, Wako, Saitama 351-0198, Japan
[37] X-ray Astrophysics Laboratory, NASA Goddard Space Flight Center, Greenbelt, MD 20771, USA
[38] Yamagata University,1-4-12 Kojirakawa-machi, Yamagata-shi 990-8560, Japan
[39] Osaka University, 1-1 Yamadaoka, Suita, Osaka 565-0871, Japan
[40] International Center for Hadron Astrophysics, Chiba University, Chiba 263-8522, Japan
[41] Institute for Astrophysical Research, Boston University, 725 Commonwealth Avenue, Boston, MA 02215, USA
[42] Department of Physics and Astronomy and Space Science Center, University of New Hampshire, Durham, NH 03824, USA
[43] Physics Department and McDonnell Center for the Space Sciences, Washington University in St. Louis, St. Louis, MO 63130, USA
[44] Istituto Nazionale di Fisica Nucleare, Sezione di Napoli, Strada Comunale Cinthia, 80126 Napoli, Italy
[45] Université de Strasbourg, CNRS, Observatoire Astronomique de Strasbourg, UMR 7550, 67000 Strasbourg, France
[46] MIT Kavli Institute for Astrophysics and Space Research, Massachusetts Institute of Technology, 77 Massachusetts Avenue, Cambridge, MA 02139, USA
[47] Graduate School of Science, Division of Particle and Astrophysical Science, Nagoya University, Furo-cho, Chikusa-ku, Nagoya, Aichi 464-8602, Japan
[48] Hiroshima Astrophysical Science Center, Hiroshima University, 1-3-1 Kagamiyama, Higashi-Hiroshima, Hiroshima 739-8526, Japan
[49] Department of Physics and Astronomy, Louisiana State University, Baton Rouge, LA 70803, USA
[50] Department of Physics, University of Hong Kong, Pokfulam, Hong Kong
[51] Université Grenoble Alpes, CNRS, IPAG, 38000 Grenoble, France
[52] Center for Astrophysics, Harvard & Smithsonian, 60 Garden St, Cambridge, MA 02138, USA
[53] INAF Osservatorio Astronomico di Brera, via E. Bianchi 46, 23807 Merate (LC), Italy
[54] Dipartimento di Fisica e Astronomia, Università degli Studi di Padova, Via Marzolo 8, 35131 Padova, Italy
[55] Department of Astronomy, University of Maryland, College Park, Maryland 20742, USA
[56] Anton Pannekoek Institute for Astronomy & GRAPPA, University of Amsterdam, Science Park 904, 1098 XH Amsterdam, The Netherlands
[57] Guangxi Key Laboratory for Relativistic Astrophysics, School of Physical Science and Technology, Guangxi University, Nanning 530004, China

Table A.1. Optical polarization of J0243 as observed with DIPol-2 in three filters *B*, *V*, and *R* in 2017.

	B		*V*		*R*	
HJD	q (%)	u (%)	q (%)	u (%)	q (%)	u (%)
			Observed polarization			
2458032.0946	−2.98 ± 0.11	−2.40 ± 0.11	−2.80 ± 0.06	−2.25 ± 0.06	−2.92 ± 0.06	−2.32 ± 0.06
2458033.0532	−3.23 ± 0.08	−2.22 ± 0.08	−3.02 ± 0.08	−2.18 ± 0.08	−2.98 ± 0.03	−2.29 ± 0.03
2458034.0270	−2.99 ± 0.08	−2.31 ± 0.08	−3.06 ± 0.05	−2.25 ± 0.05	−2.96 ± 0.03	−2.19 ± 0.03
2458037.0155	−3.07 ± 0.07	−2.13 ± 0.07	−2.97 ± 0.05	−2.31 ± 0.05	−2.92 ± 0.03	−2.27 ± 0.03
2458038.0295	−2.96 ± 0.05	−2.20 ± 0.05	−3.09 ± 0.04	−2.22 ± 0.04	−2.98 ± 0.03	−2.25 ± 0.03
2458043.9848	−2.91 ± 0.08	−2.03 ± 0.08	−2.88 ± 0.12	−2.28 ± 0.12	−2.87 ± 0.04	−2.17 ± 0.04
2458044.9984	−2.69 ± 0.04	−1.95 ± 0.04	−2.95 ± 0.04	−2.12 ± 0.04	−2.84 ± 0.03	−2.30 ± 0.03
2458045.9972	−2.94 ± 0.05	−2.32 ± 0.05	−3.02 ± 0.05	−2.18 ± 0.05	−2.88 ± 0.03	−2.20 ± 0.03
2458048.0195	−3.10 ± 0.06	−2.13 ± 0.06	−3.19 ± 0.04	−2.08 ± 0.04	−2.95 ± 0.03	−2.17 ± 0.03
2458053.9188	−3.03 ± 0.05	−2.46 ± 0.05	−3.08 ± 0.04	−2.22 ± 0.04	−2.86 ± 0.02	−2.37 ± 0.02
2458054.9985	−2.93 ± 0.04	−2.41 ± 0.04	−3.09 ± 0.03	−2.17 ± 0.03	−2.94 ± 0.02	−2.16 ± 0.02
2458056.0199	−3.02 ± 0.03	−2.26 ± 0.03	−3.03 ± 0.03	−2.20 ± 0.03	−2.93 ± 0.02	−2.24 ± 0.02
2458057.0056	−2.97 ± 0.04	−2.30 ± 0.04	−3.02 ± 0.04	−2.20 ± 0.04	−2.99 ± 0.03	−2.24 ± 0.03
2458058.0394	−3.14 ± 0.08	−2.12 ± 0.08	−2.95 ± 0.07	−2.33 ± 0.07	−2.87 ± 0.03	−2.31 ± 0.03
2458060.9934	−3.01 ± 0.05	−2.18 ± 0.05	−2.94 ± 0.04	−2.26 ± 0.04	−2.89 ± 0.02	−2.29 ± 0.02
2458062.9920	−3.02 ± 0.06	−2.17 ± 0.06	−2.98 ± 0.04	−2.14 ± 0.04	−2.92 ± 0.02	−2.27 ± 0.02
2458063.9987	−3.09 ± 0.05	−2.28 ± 0.05	−3.03 ± 0.04	−2.22 ± 0.04	−2.97 ± 0.02	−2.29 ± 0.02
2458064.9702	−2.94 ± 0.03	−2.41 ± 0.03	−3.05 ± 0.03	−2.24 ± 0.03	−2.95 ± 0.02	−2.34 ± 0.02
2458065.9628	−2.92 ± 0.06	−2.19 ± 0.06	−3.02 ± 0.04	−2.14 ± 0.04	−2.96 ± 0.02	−2.30 ± 0.02
2458067.9801	−2.73 ± 0.03	−2.28 ± 0.03	−2.95 ± 0.04	−2.30 ± 0.04	−2.84 ± 0.02	−2.34 ± 0.02
2458070.9535	−3.14 ± 0.04	−2.35 ± 0.04	−3.05 ± 0.03	−2.26 ± 0.03	−2.93 ± 0.02	−2.26 ± 0.02
2458071.9512	−2.99 ± 0.04	−2.29 ± 0.04	−3.03 ± 0.04	−2.37 ± 0.04	−2.89 ± 0.02	−2.33 ± 0.02
2458074.9499	−3.06 ± 0.05	−2.23 ± 0.06	−3.02 ± 0.04	−2.21 ± 0.04	−2.91 ± 0.02	−2.35 ± 0.02
2458075.9985	−3.17 ± 0.05	−2.30 ± 0.05	−2.97 ± 0.04	−2.29 ± 0.04	−2.89 ± 0.02	−2.41 ± 0.02
2458077.8976	−3.05 ± 0.05	−2.10 ± 0.05	−2.96 ± 0.06	−2.39 ± 0.06	−2.82 ± 0.03	−2.32 ± 0.03
2458078.9242	−3.00 ± 0.05	−2.31 ± 0.05	−2.94 ± 0.03	−2.32 ± 0.03	−2.84 ± 0.02	−2.32 ± 0.02
2458079.8771	−3.00 ± 0.04	−2.21 ± 0.04	−2.97 ± 0.03	−2.26 ± 0.03	−2.86 ± 0.02	−2.41 ± 0.02
2458081.9241	−3.01 ± 0.06	−2.25 ± 0.06	−3.01 ± 0.05	−2.22 ± 0.05	−2.88 ± 0.02	−2.36 ± 0.02
2458091.9003	−3.07 ± 0.07	−2.16 ± 0.07	−3.00 ± 0.05	−2.15 ± 0.05	−2.93 ± 0.03	−2.27 ± 0.03
2458093.8934	−3.04 ± 0.07	−2.03 ± 0.07	−3.08 ± 0.05	−2.20 ± 0.05	−2.87 ± 0.03	−2.31 ± 0.03
2458094.9295	−3.11 ± 0.06	−2.13 ± 0.06	−3.06 ± 0.06	−2.23 ± 0.06	−2.90 ± 0.02	−2.31 ± 0.02
2458096.8955	−3.05 ± 0.05	−2.26 ± 0.05	−3.04 ± 0.05	−2.22 ± 0.05	−3.00 ± 0.02	−2.26 ± 0.02
2458097.8895	−3.08 ± 0.05	−2.22 ± 0.05	−3.04 ± 0.04	−2.21 ± 0.04	−3.02 ± 0.02	−2.28 ± 0.02
2458101.8661	−3.08 ± 0.05	−2.13 ± 0.05	−2.91 ± 0.04	−2.31 ± 0.04	−2.87 ± 0.02	−2.38 ± 0.02
2458112.8621	−2.85 ± 0.04	−2.21 ± 0.04	−3.03 ± 0.05	−2.27 ± 0.05	−2.91 ± 0.02	−2.29 ± 0.02
Average observed	−2.99 ± 0.01	−2.25 ± 0.01	−3.012 ± 0.007	−2.234 ± 0.007	−2.908 ± 0.004	−2.302 ± 0.004
			Interstellar polarization			
Star #3	−3.67 ± 0.40	−3.82 ± 0.40	−2.79 ± 0.30	−3.31 ± 0.30	−2.81 ± 0.20	−3.11 ± 0.20
			Intrinsic polarization			
	0.68 ± 0.40	1.57 ± 0.40	−0.22 ± 0.30	1.1 ± 0.3	−0.1 ± 0.2	0.8 ± 0.2
	PD (%)	PA (deg)	PD (%)	PA (deg)	PD (%)	PA (deg)
	1.7 ± 0.4	33 ± 7	1.1 ± 0.3	51 ± 8	0.8 ± 0.2	49 ± 7

Notes. Normalized Stokes parameters q and u are presented for the observed optical polarization of the source, the interstellar (IS) polarization, and the intrinsic polarization obtained by subtracting the IS polarization from the observed values. The PD and PA χ_o of the intrinsic optical polarization are computed from the intrinsic q and u. Uncertainties are 1σ.

Appendix A: Optical polarimetric observations during 2017 outburst

Table A.1 presents the results of the optical polarimetric measurements of J0243 during its 2017 outburst obtained with DIPol-2 (Piirola et al. 2014) at the T60 telescope at Haleakala, Hawaii. Polarization of the field star #3 (see Fig. 6) was determined using observations in February 2024 at the same telescope.